

Micrometer-sized ice particles for planetary-science experiments – II. Bidirectional reflectance

Bernhard Jost^{a,*}, Bastian Gundlach^b, Antoine Pommerol^a, Joachim Oesert^c, Stanislav N. Gorb^c, Jürgen Blum^b, Nicolas Thomas^a

^a Physikalisches Institut, Universität Bern, Sidlerstrasse, 5, CH-3012 Bern, Switzerland

^b Institut für Geophysik und extraterrestrische Physik, Technische Universität Braunschweig, Mendelssohnstr. 3, D-38106 Braunschweig, Germany

^c Zoologisches Institut, Christian-Albrechts-Universität zu Kiel, Am Botanischen Garten 1-9, D-24118 Kiel, Germany

ARTICLE INFO

Article history:

Received 18 September 2012

Revised 5 April 2013

Accepted 8 April 2013

Available online 22 April 2013

Keywords:

Comets

Experimental techniques

Ices

Photometry

Satellites, Surfaces

ABSTRACT

We have measured the bidirectional reflectance of spherical micrometer-sized water-ice particles in the visible spectral range over a wide range of incidence and emission angles. The small ice spheres were produced by spraying fine water droplets directly into liquid nitrogen. The resulting mean particle radii are $1.47 + 0.96 - 0.58 \mu\text{m}$. Such a material shares many properties with ice in comets and at the surface of icy satellites. Measurements show that the fresh sample material is highly backscattering, contrasting with natural terrestrial snow and frost. The formation of agglomerates of particles during the sample production results in a noticeable variability of the photometric properties of the samples in their initial state. We have also observed significant temporal evolutions of the scattering behavior of the samples, shifting towards more forward scattering within some tens of hours, resulting most likely from sintering processes. All reflectance data are fitted by the Hapke photometric model (1993 and 2002 formulation) with a one/two/three-parameter Henyey–Greenstein phase function and the resulting Hapke parameters are provided. These parameters can be used to compare laboratory results with the observed photometric behaviors of astronomical objects. We show, in particular, that the optical properties of the fresh micrometer-sized ice samples can be used to reproduce the predominant backscattering in the phase curves of Enceladus and Europa.

© 2013 Elsevier Inc. All rights reserved.

1. Introduction

Water ice played an important role during the formation of the Solar System as can be seen by the high water ice abundances in the outer Solar System. Coagulation models assume a higher specific surface energy for water ice than for refractory materials (Wada et al., 2008). The increased specific surface energy of water ice over the refractory materials is a key parameter in models of the formation of the giant planets, their satellite systems and comets. However, most of these bodies were processed after formation by metamorphism or melting. The only exceptions are probably comets and objects in the Cold Classical Kuiper Belt, which have never experienced high temperatures or pressures after their formation.

The first evidence for the presence of micrometer-sized water ice particles in comets was provided by the Deep Impact mission (A'Hearn et al., 2005). After the collision of the impactor with Comet 9P/Tempel, micrometer-sized water ice particles were

observed in the plume by analyzing the infrared absorption bands of the ejected material (Sunshine et al., 2007). Additionally, micrometer-sized water ice particles were also observed in the innermost coma of the highly active Comet 103P/Hartley 2, during the flyby of the EPOXI mission (A'Hearn et al., 2011).

Near-infrared spectra show the presence of water frost or ice on the surface of Saturn's moon Enceladus with strong indications that the size distribution is dominated by particles sizes of some tens of microns (Cruikshank et al., 1977; Hansen and McCord, 2004; Emery et al., 2005; Verbiscer et al., 2006; Filacchione et al., 2007, 2010; Jaumann et al., 2008; Hansen and Romain, 2012). Water ice particles of similar size were also detected close to Enceladus' surface where they form from outstreaming water vapor (Schmidt et al., 2008). Furthermore, Enceladus is the source of E-ring particles as can be seen by the size distribution of these particles and by the spatial density distribution of the E-ring (Cruikshank et al., 1977; Showalter et al., 1991; Nicholson et al., 1996).

In a previous first publication, it was demonstrated how micrometer-sized water ice particles can be produced in the laboratory (Gundlach et al., 2011; hereafter called paper I). It was found that the specific surface energy of water ice particles is

* Corresponding author.

E-mail address: bernhard.jost@space.unibe.ch (B. Jost).

approximately ten times higher than the specific surface energy of SiO_2 , which illustrates again the unusual properties of water.

Optical methods such as visible imaging, infrared spectrometry and spectro-imaging, are among the most widely used remote-sensing techniques. In addition to the spatial dimensions used for imaging and spectral dimension used for spectrometry, the dependence of the reflectivity of the studied object on the geometry of the measurement, i.e. the positions of the light source and the detector, can provide additional constraints on the composition and physical state of the surface. The angle between the incidence and emission directions, the phase angle, is the most important of the geometric parameters. Phase curves, the relationships between reflectance and phase angle, are regularly measured for a variety of Solar System objects from Earth-based observatories and by spacecraft.

Particularly relevant for this work are the photometric measurements of the icy satellites of Jupiter and Saturn using the cameras and spectrometers on both Voyager spacecrafts, Galileo and Cassini, complemented by Earth-based telescopic observations (Domingue et al., 1991; Buratti, 1995; Domingue and Verbiscer, 1997; Rodriguez et al., 2007; Newman et al., 2008; Hendrix and Buratti, 2009). In the case of comets, interesting photometric measurements were acquired by the Deep Impact/EPOXI and Stardust spacecraft (A'Hearn et al., 2011; Li et al., 2009). In the first half of 2014, the OSIRIS imaging system onboard ESA's Rosetta spacecraft will start acquiring images of the nucleus of Comet 67P/Churyumov–Gerasimenko. As the spacecraft will fly around the comet over the course of several months, it will be possible to determine the photometric properties of the nucleus materials with unprecedented accuracy. In order to be able to retrieve physical properties from these photometric properties, it is important to assess the accuracy of currently existing photometric models and build libraries of the photometric properties of well-characterized laboratory analogs for cometary material.

Physical models have been developed and used for decades to establish relationships between the bidirectional reflectance of a given object, the intrinsic optical properties of its individual component and, the macroscopic properties of the surface. The most popular model in the planetary community is the one developed by Hapke (1981, 1986, 1993, 2002), simply referred to as “Hapke model” in the rest of this manuscript, which is based on the application of radiative transfer theory to the case of particulate surfaces. This model has been extensively tested in the laboratory using both natural materials and test samples. Recent summaries of the strengths and weaknesses of the model are provided by Gunderson et al. (2006, 2007), Shepard and Helfenstein (2007, 2011), Hapke et al. (2009), Helfenstein and Shepard (2011) and Souchon et al. (2011).

Although water ice is one of the main constituents of the surfaces of many Solar System objects, its photometric properties have not been as extensively characterized as other planetary analogs, minerals and organics. Challenges in working with this material involve the need for devices operating in cold rooms, coping with the rapid temporal evolution of ice surfaces and the difficulty in obtaining *in situ* complementary characterizations. Extensive measurements of the reflectance of different types of snow have been acquired in the past (Middleton and Mungall, 1952; Dumont et al., 2010 and references therein). They all show a strongly anisotropic scattering of light by this material with, in particular, a maximum of scattered light in the forward direction (“forward scattering” behavior). The photometric properties of different types of snow have been compared in the past to those of the saturnian and uranian satellites (Verbiscer and Veverka, 1990) and the Galilean satellites (Domingue et al., 1997). Verbiscer et al. (1990) also compared Hapke parameters of terrestrial snows and frost to those of saturnian and uranian satellites and Europa.

The significant differences in photometric behavior between the surfaces of the icy satellites and terrestrial snow samples were attributed to differences in particle structure and textures.

Whereas measurements of snow and other forms of water ice naturally found on Earth are crucial for the terrestrial remote-sensing community, they are not sufficient for the study of other Solar System objects. The different forms that water ice can take, depending on the mechanism of formation and metamorphism under variable environmental conditions, strongly influence its photometric properties and it is, thus, hard to assume that any terrestrial occurrence of water ice will behave as the ice found in cometary nuclei or the surface of Enceladus, for example.

Working with synthetic analogs of water ice, such as glass beads, is a way to bypass most of the difficulties that occur with water ice. This allows validation of the physical models for very transparent materials (Hapke et al., 2009; Zhang and Voss, 2011). However, the natural complexity of ice is hard to reproduce accurately with synthetic materials and the influence of its metamorphism on its photometric behavior, a major topic of interest in planetary science, cannot be characterized.

In this work, we report on visible bidirectional reflectance measurements of micrometer-sized water ice particles (see Gundlach et al., 2011). All measurements were performed with the PHIRE-2 gonio-radiometer in the Planetary Ice Laboratory at University of Bern (Pommerol et al., 2011; see Section 2). The sample preparation is described and the sample properties are reviewed in Section 3. In Section 4, the measured bidirectional reflectance of the micrometer-sized water ice particles is presented. The experimental data were fitted by the Hapke model (Hapke, 1993, 2002) and the resulting model parameters are provided. These can mainly be used to compare with planetary observations (see Section 5). Finally, we conclude this paper by reviewing the main results of this work (see Section 6).

2. Methods

2.1. Photometric measurements

All photometric measurements reported in this paper were conducted with the PHIRE-2 (PHysikalisches Institut Radiometric Experiment – 2), the second generation of gonio-radiometers developed at the University of Bern for planetary sciences applications (see Pommerol et al., 2011 for details).

Schematically, the PHIRE-2 instrument consists of a cylindrical sample holder (diameter: 160 mm, height: 200 mm) surrounded by two mobile arms. One holds a collimated light source and the other a light detector. The positions of the light source and the detector can be varied in order to obtain different illumination and viewing geometries.

The position of the light source relative to the sample is described by the incidence angle, i . When the light source is vertical ($i = 0^\circ$), a circular area in the middle of the sample is illuminated. The diameter of the illuminated area can be varied between a few millimeters and 3 cm. The selection of the aperture depends on the optical properties, the surface texture and the available amount of sample material. In this work, a spot diameter of 10 mm was chosen. For increasing incidence angles, the illuminated area becomes ellipsoidal. The length of the ellipse, L , is proportional to $\cos(i)$. Thus, the size of the sample eventually limits the maximum incidence angle that can be reached.

The position of the detector relative to the sample is described by the emission angle e and the azimuth angle a . The angle between the incidence and emission directions is the “phase angle” g and the vertical plane containing the incidence direction is called “principal plane”. For $a = 0^\circ$, the emission direction is contained in

the principal plane. The arm holding the detector interferes with the light beam emitted from the source at low phase angle by design. This restricts the measurements to phase angles larger than 4° .

A 250 W tungsten–halogen lamp is used as a light source and an amplified Si photodiode is used as the detector. In this configuration, PHIRE-2 measures the reflectance of samples over the visible and near-infrared spectral range (400–1100 nm). A motorized filter wheel equipped with six bandpass filters allows the selection of restricted wavelength ranges, centered around 450 nm, 550 nm, 650 nm, 750 nm, 905 nm and 1064 nm with full width at half maximum bandwidths of either 70 nm (for 450–750 nm) or 25 nm (for 905 nm and 1064 nm).

The absolute calibration of the experiment is performed by normalizing the measured reflectance values to the reflectance measured for a reference surface (Spectralon™, Labsphere Inc.) which is illuminated vertically and observed at $e = 55^\circ$ (see Gunderson et al., 2007 for details). Using this method, the reflectance data are calibrated in units of “reflectance factor”, the ratio between the actual reflectance of the sample measured in a particular geometry and the one of a hypothetical perfect Lambertian diffuser measured in the same geometry ($I/[F \cdot \cos(i)]$). A comparison of different calibration measurements performed with different instruments (Pommerol et al., 2011) indicates an absolute calibration accuracy of about $\pm 1\%$. Long timescale calibration measurements (~ 10 h) also show a long-term stability of the measured reflectance within this range. According to Fermat’s principle the reflectance value should be identical when the positions of light source and detector are permuted (e.g. $i = 0^\circ$, $e = 40^\circ$ and $i = 40^\circ$, $e = 0^\circ$). Comparisons of all possible permutations indicate errors within the range of 0.4–1.0% for single data points.

A time-independent systematic error is produced by the uneven movement of the sensor arm for $e = 0^\circ$ to $e = +75^\circ$. This inaccuracy causes variations of 0.5% of the signal. Because of the $\cos(e)$ dependence of the signal value (Gunderson et al., 2006), the maximum influence takes place at high emission angles. Thus, the error is 2% for a measurement conducted at $e = 75^\circ$. For $i = 40^\circ$ and 60° this mechanical effect is less visible because the absolute variations in reflectance are much higher for high phase angles. Another hardware artifact occurs sometimes at $e = +35^\circ$ and causes an increase or a decrease of the signal by up to 50%. We have not found the exact reason yet but suspect a mechanical resonance. The associated erroneous data are excluded in all analyses.

An important requirement for accurate photometric measurements is the need to have samples that are large enough to be considered as optically thick or semi-infinite, i.e. the photons cannot reach the boundaries of the sample. In addition to their intrinsic optical properties, the size of the individual particles also determines the required sample thickness. According to Hapke (1993), a thickness of sample $h = 66/\phi \cdot d$ is required for samples having a single scattering albedo of 1. Here, ϕ is the volumetric filling factor of the bulk samples and d is the diameter of the individual particles. The optical opacity of a sample can be easily assessed by comparing the apparent reflectance of different thicknesses of the same sample. The sample can be considered as optically thick if the reflectance does not depend on the thickness h .

The PHIRE-2 instrument is installed in a large laboratory freezer in which the temperature can be set to any value between $T = 238$ K and $T = 258$ K. When operated at $T = 238$ K (all measurements in this paper), the compressor is constantly running and cold dry air is continuously blown from the top of the freezer to the bottom of the freezer, ensuring stable and homogenous conditions, with a nearly constant temperature of the sample holder ($T = 239 \pm 1.5$ K) and a nearly constant relative humidity ($\text{RH} = 48 \pm 2\%$). The temperature at four different heights in the

freezer and the relative humidity close to the sample were constantly monitored during all experiments. For technical reasons, the compressor of the freezer turns off every 4 h for 5 min. During this time, the air temperature increases to about 244 K, but the temperature of the sample holder is not significantly affected. After this period, the air temperature decreases to a temperature of $T = 239$ K in 10 min. Additionally, the relative humidity shortly rises up to $65 \pm 2\%$, then decreases down to $48 \pm 2\%$ in 15 min.

The PHIRE-2 is entirely controlled by a single computer that allows programming a series of measurements that are repeated over time. In this context, the term “time resolution” is the interval of time after which the entire sequence of measurements is repeated. A typical sequence of measurements consisted of 4 “2D” scans in the principal plane ($a = 0^\circ$) with emission angle ranging from -80° to $+80^\circ$ (increment: 5°). The incidence angle was kept constant during each of the four scans at $i = 0^\circ$, 20° , 40° and 60° , respectively. However, due to the limitations given by the mechanical inaccuracies, the maximum emission angle at which we acquired useful data was $e = 70^\circ$. The smallest phase angle at which measurements were obtained is thus 5° and the largest 130° . Depending on the sample, measurements were conducted either at multiple wavelengths or at a single wavelength to improve the time resolution.

2.2. Fitting of experimental data by the Hapke photometric model

The measured reflectance curves were fitted using the bidirectional reflectance model developed by Hapke (1993/2002; “Hapke model”). This model attempts to relate the optical properties of single isolated particles with the bidirectional reflectance of a solid dense surface composed of these particles. The intrinsic optical properties of the particles considered in the model are the single scattering albedo, ω_0 , and the single scattering phase function. The latter property is classically described mathematically by a Henyey–Greenstein function (Henyey and Greenstein, 1941) with one, two or three free parameters. The one parameter Henyey–Greenstein function has the form,

$$p(g) = \frac{1 - b^2}{(1 + 2 \cdot b \cdot \cos(g) + b^2)^{3/2}} \quad (1)$$

where g is the phase angle and b ($-1 < b < 1$) the Henyey–Greenstein parameter which represents the average cosine of the scattering angle. The two parameter phase function separates into a forward and a backward scattering fraction and has the form (McGuire and Hapke, 1995):

$$p(g) = \frac{1 + c}{2} \frac{1 - b^2}{(1 - 2 \cdot b \cdot \cos(g) + b^2)^{3/2}} + \frac{1 - c}{2} \times \frac{1 - b^2}{(1 + 2 \cdot b \cdot \cos(g) + b^2)^{3/2}} \quad (2)$$

The parameter ranges are $0 < b < 1$ and $-1.5 < c < 2.5$. The phase function with 3 free parameters separately treats the angular widths of the forward and backward scattering lobes:

$$p(g) = \frac{1 + c}{2} \frac{1 - d^2}{(1 - 2 \cdot d \cdot \cos(g) + d^2)^{3/2}} + \frac{1 - c}{2} \times \frac{1 - b^2}{(1 + 2 \cdot b \cdot \cos(g) + b^2)^{3/2}} \quad (3)$$

Its parameter ranges are $0 < b < 1$, $-1.5 < c < 2.5$ and $0 < d < 1$. In addition to these classical definitions, we have also fitted the data using a 2 parameters Henyey–Greenstein phase function (Eq. (2)) assuming that the b and c parameters are related by the empirical

“Hockey stick relation” (Eq. (4)) determined and described in details by Hapke (2012).

$$c = 3.29 \exp(-17.4b^2) - 0.908 \quad (4)$$

We warn the reader that different definitions of the Henyey–Greenstein functions and parameters have been used in the literature and it is therefore particularly important to clearly identify which form of the function is used and how the parameters are defined.

While the 1993 formulation of the Hapke model makes the approximation of an isotropic multiple scattering (only the first scattering is considered anisotropic), an improved version (Hapke, 2002) incorporates anisotropic multiple scattering, which is potentially necessary for high albedo samples. In this work, we fitted multiple combinations of single scattering phase functions and models. The 1993 formulation was used with 1-, 2- and 3-parameter Henyey–Greenstein functions and the “Hockey stick relation” (Hapke, 2012). The isotropic multiple scattering version of the model (Hapke, 1986, 1993) was always used with the improved approximation of the Ambartsumian–Chandrasekhar *H*-function defined in Hapke (2002).

The 2002 model formulation was only used with the 2-parameter Henyey–Greenstein function, because the 3-parameter function produces extreme sensitivity to numerical problems during calculation of the multidimensional integrations.

In the 1993 version of the Hapke model, 2 parameters are used to describe the shape and amplitude of the opposition surge, i.e. the strong increase of reflectance at low phase angle. The amplitude of the opposition peak is defined by the B_0 parameter while its angular width is defined by the h parameter, which is physically related to the compaction of the sample. The subsequent version of the model (Hapke, 2002) uses more accurate physical descriptions of the two mechanisms that cause the Opposition Effect (OE): Shadow Hiding (SHOE) and Coherent Backscattering (CBOE). We completely neglected Coherent Backscattering in our analysis because its angular half-width is about 2° , while the lowest phase angle measured here is 5° . The CBOE model parameters are fixed in our data fitting and set to 0.

The last Hapke model parameter, θ , describes the macroscopic roughness of the sample. It is defined as the average tilt angle of the surface, in degrees. The Hapke model that we fit to the measured reflectance data thus has 5–7 free parameters, depending on the number of free parameters of the Henyey–Greenstein single scattering phase function.

We found that a two-step fitting procedure is the most efficient way to fit the model to measured data. In a first step, we use a Particle Swarm Optimization (PSO) strategy (Kennedy and Eberhart, 1995) that has previously successfully been applied to photometric data of meteorites samples measured on the PHIRE-2 by Beck et al. (2012). We only run the PSO for about 50 iterations, with a particle number of 100, which is not sufficient to obtain a satisfactory fit but provides a good initial guess of the set of Hapke parameters. A Levenberg–Markwardt algorithm (MPFIT, Markwardt, 2008), was then used in a second step. The combination of these two techniques considerably decreases the time needed for the entire fitting procedure compared to the procedure used by Beck et al. (2012) and allows better reproducibility of the retrieved parameters. The final difference between the fitted model and the measured data is expressed by the root mean square (RMS) i.e.

$$\text{RMS} = \sqrt{\frac{\sum_i^N (D_i - M_i)^2}{N}} \quad (5)$$

where D is the measured data and M the modeled value at the same incidence, emission and phase angles. Another common and useful

criterion to quantify the goodness of the fit is the reduced chi-square value (χ_v^2) which is defined as

$$\chi_v^2 = \frac{\sum_i^N (D_i - M_i)^2}{\sigma \cdot (N - n)} \quad (6)$$

where σ is the uncertainty of a single data point (in our case a relative uncertainty of 0.01, see Section 2.1) and n is the number of free parameters (5–7). A χ_v^2 -value of 1 theoretically represents a perfect fit of a dataset, while higher values indicate inadequacies in the model used to fit data. Values between 1 and 0 mean that the model is “overfitting” the data and might be influenced by signal noise and instrumental artifacts.

A major reason to continue to use the older 1993 isotropic multiple scattering approximation (besides its wide spread use in the community) is the calculation time, which is by far shorter than the more accurate 2002 version. A good way to save time is to run the PSO with the old version of the model and the much faster MPFIT method with the improved version.

It is well known that fitting photometric phase curves with the Hapke model leads to non-unique results because the individual parameters are strongly coupled and compensate changes in other parameters (Gunderson et al., 2006). To estimate the uncertainties on the model parameters, we use the same method as used by Johnson et al. (2006) to establish a 1σ -confidence interval. Starting from the optimal set of Hapke parameter found by our fitting procedure, one parameter is varied by incremental steps around its best-fit value while other parameters are re-fitted and allowed to compensate the deviation. The resulting χ_v^2 values display curves with clear minima for well constrained parameters and low gradients for poorly constrained parameters. The 1σ confidence interval is defined between the two points where the χ_v^2 -curve reaches a value of $\chi_{v,\min}^2 + 1$. This corresponds to a degradation of the goodness of fit by a level equivalent to the uncertainty on measured values.

We found that some of the parameters are well constrained towards one direction in parameter space but completely unconstrained towards the other. The resulting intervals of the Hapke model parameters are $+0.0014/-0.0005$ for ω_0 , $-0.34/+0.41$ for B_0 , -0.13 for h , $+4^\circ$ for θ . There is no upper limit for h and no lower limit for θ . In the case of a 1-parameter Henyey–Greenstein function the parameter b has a confidence interval of ± 0.04 , in the case of a 2-parameter HG function, the confidence interval for b is: $-0.14/+0.07$ and c only has a upper limit: $+0.15$. For the 3-parameter HG-function all 3 parameters are totally unconstrained.

3. Samples preparation and characterization

3.1. Preparation

In the current work, a slightly different setup for the sample preparation was used than in paper I (Gundlach et al., 2011). As shown in Fig. 1, liquid water was dispersed by an inhalator of type Pari Boy SX (1) and sprayed directly into liquid nitrogen (2), which was stored in a custom-made Dewar vessel (3). After the production of a sufficient amount of water ice particles, a valve (4), located beneath the liquid nitrogen reservoir, was opened to extract the particles. Following extraction, the particles were filled, together with a small amount of liquid nitrogen, into a transport container (5).

The produced water ice particles were then carried to a freezer, in which the preparation of the final sample was performed. There, the micrometer-sized water ice particles were filled into the sample holder of the gonio-radiometer using a spatula. Both the spatula and the sample holder of the gonio-radiometer had previously been cooled to the temperature of the preparation freezer (250 K).

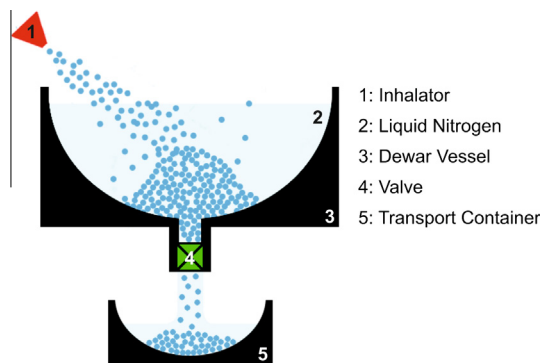


Fig. 1. Schematic diagram of the setup that was used for the production of the micrometer-sized water ice particles. Liquid water was dispersed by an inhalator (1) and then sprayed into liquid nitrogen (2), which was stored in a Dewar vessel (3). Afterwards, a valve (4) was opened to extract the water ice particles. The water ice particles were then filled into a transport container (5) for further experiments.

When transferred into the sample holder, the microscopic ice particles formed mm-sized agglomerates. The surface of the sample was then leveled to the rim using a spatula in order to obtain a horizontal and flat surface. Care was taken to ensure that the sample was not compacted during preparation. The sample preparation was performed quickly (<1 min) to minimize potential sintering of the sample prior to the start of photometric measurements.

After preparation, the sample was transferred to the gonio-radiometer, which was actively cooled to 238 K (see Section 2.1). During the transfer, the surface of the sample was covered by a lid to minimize condensation of frost on the sample's surface. Both transfers, the transfer from the Dewar vessel to the freezer and the transfer from the freezer to the gonio-radiometer were conducted very quickly, within less than 10 s.

Because very fine-grained samples were used in this study, it was possible to use a relatively small holder (see discussion in Section 2). We selected a sample holder of dimensions 50 mm × 20 mm × 5 mm (volume = 5 cm³) for all measurements. 2 h were necessary to produce the amount of sample necessary to fill the sample holder. Assuming a filling factor of $\phi = 0.25$, the necessary thickness for a semi-infinite sample (Hapke, 1993) is 264 monolayers which corresponds to 400 μm . This leads to a comfortable margin of one order of magnitude.

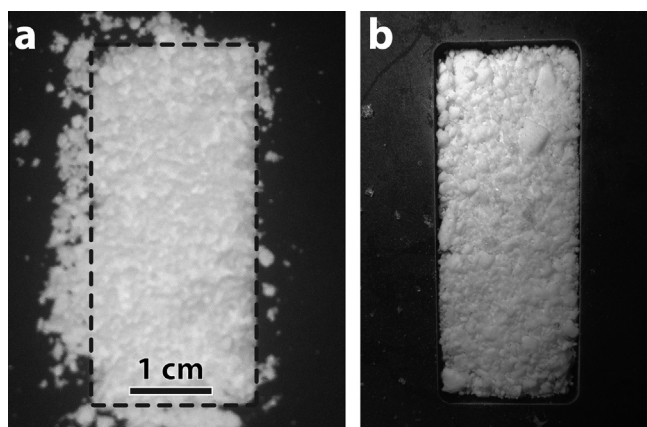


Fig. 2. Pictures of sample C in the sample holder before (a) and after (b) the series of photometric measurements. Both pictures were taken 70 h apart. During that time, the sample was kept at a nearly constant temperature of 238 K and a nearly constant relative humidity of 48%. The sample experienced significant sublimation and sintering as revealed by obvious volume loss and appearance of large agglomerates. On picture a, the black dashed line shows the extent of the inner part of the sample holder, otherwise partially hidden by ice deposited around.

3.2. Macroscopic texture

Fig. 2a shows a picture of a typical sample (sample C) taken just a few seconds after sample preparation. Despite the flattening with the spatula, the initial material shows a high surface roughness. Small particles actually form millimeter-sized agglomerates during surface preparation. It is interesting to note that the small particles of ice deposited around the sample holder appear as bright as the surface of the sample itself. It proves that, as expected from theory, less than a millimeter is required for the sample to be optically thick. Fig. 2b is a picture of the same sample taken 70 h later. The sample experienced significant sublimation and sintering as revealed by obvious volume loss and appearance of large agglomerates. Effects of sublimation and sintering on the texture and photometric properties of the sample are presented and discussed in detail in Sections 4 and 5.

3.3. Volume filling factor

The volume filling factor of the samples was estimated by accurately measuring the mass of a known volume of the material. A container of 5 cm³ was entirely filled with freshly produced sample material, prepared in the exact same way as for the photometric measurements (see Section 3.1). Note that the samples used for volume filling factor measurements are not the ones we used for photometric measurements, as the mass measurement had to be made under ambient laboratory conditions. The mass, about 1 g, was determined by a mg-resolution laboratory scale (Denver Instruments, Si-603). The whole procedure was repeated three times, each time with a newly produced sample. Using a density of $\rho = 0.92 \text{ g/cm}^3$ for water ice at $T = 239 \text{ K}$ yields volume filling factors of $\phi = 0.24$, $\phi = 0.23$ and $\phi = 0.27$. The slight variability is assumed to originate from the variable compaction of the material during insertion into the container.

3.4. Microscopic structure

The particle size and microscopic structure of the micrometer-sized water ice particles was investigated with a cryogenic cooled scanning electron microscope (SEM) at the University of Kiel. A detailed description of the microscope can be found in Voigt and Gorb (2010) and references therein. For the observations with the SEM, the samples were prepared exactly as described in Section 3.1.

Using the SEM, it was possible to investigate the structure of the micrometer-sized water ice particles on a micrometer scale. Examples of the water ice particles, as observed with the cryogenic cooled SEM, are shown in Fig. 3. The micrometer-sized water ice particles are visibly spherical. The SEM images were used to measure the size distribution and the mean radius of the grains (see Section 3.5).

Some water ice particles were covered by frost (visible as chips on the surfaces of the grains). The condensation of frost occurred during the transfer of the sample from the Dewar vessel, where the water ice particles were produced, to the microscope. Thus, condensation of frost should also occur during the transfer of the sample from the Dewar vessel to the gonio-radiometer. However, our investigation with the cryogenic cooled SEM showed that only a thin layer of frost forms on the particles (see Fig. 3). The frost was in all cases located on the top layers of the sample and not inside the voids of the porous aggregate. A discussion of the presence of frost on the samples during the measurements of the spectral reflectance is provided in Section 5.

3.5. Size distribution

The size distribution of the micrometer-sized water ice particles was already investigated in Gundlach et al. (2011) with an optical

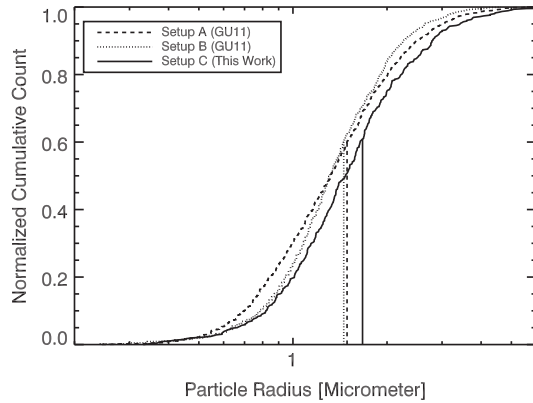


Fig. 3. Size distribution of the micrometer-sized water ice particles. The size distribution derived from the images of the cryogenic cooled SEM (log-normal size distribution, solid curve) and the size distribution, measured in the paper I (dashed and dotted curves, Gundlach et al., 2011) are shown. The resulting mean particle radii are: $r_A = 1.49 \pm 0.79 \mu\text{m}$, $r_B = 1.45 \pm 0.65 \mu\text{m}$ and $r_C = 1.47 + 0.96 - 0.58 \mu\text{m}$. The 1σ deviation of the log-normal distribution is shown by the long-dashed lines.

microscope. It was found that the mean particle radius of the water ice particles produced with the former setups is $r_A = 1.49 \pm 0.79 \mu\text{m}$ (setup A, see Fig. 4, dashed curve) and $r_B = 1.45 \pm 0.65 \mu\text{m}$ (setup B, see Fig. 4, dotted curve). The uncertainty denotes the standard deviation of the measurement of the radii.

The size distribution of the micrometer-sized water ice particles produced with the setup used in this paper (see Section 3.1) was analyzed using the images from the cryogenic cooled SEM (see Fig. 3). The resulting size distribution (log-normal distribution) is shown in Fig. 4 (solid curve). We derived the typical particle radius from the mean of the logarithm of the measured particle radii,

$r_C = 1.47 + 0.96 - 0.58 \mu\text{m}$. The previously measured log-normal size distributions match very well with the size distribution obtained from the cryogenic cooled SEM images.

4. Results

The laboratory measurements on PHIRE-2 are performed on three identically produced samples (later called A, B and C). The experimental conditions for the samples A, B and C are shown in Table 1. The measurements were regularly repeated over the course of 4 h (sample A), 35 h (sample B) and 41 h (sample C), respectively. For the samples A and B, the measurements were obtained at four different wavelengths: 450 nm, 650 nm, 750 nm and 1064 nm. In order to decrease the interval between identical measurements, and because the measurements with the first two samples did not reveal any particular effect of wavelength, we only performed measurements at 650 nm for sample C. With these parameters, we obtain temporal resolutions between 6 min and 25 min for the first hours and long-term temporal resolutions of 110 min (sample B) and 72 min (sample C).

Fig. 5 shows the comparison of the bidirectional properties of three fresh samples (the measurements were performed a few minutes after the introduction of the sample holder in the freezer). The scans were performed for four incidence angles, $i = 0^\circ$, $i = 20^\circ$, $i = 40^\circ$ and $i = 60^\circ$. Sample B was not measured at $i = 20^\circ$ to save time and thus improve the temporal resolution. The dotted lines through the data points are the results of fitting the Hapke reflectance model to the data (see Section 2.2). Despite very similar preparation procedures, we note a significant variability in the photometric behavior of the three samples. Particularly remarkable is the difference between samples A and C at low phase angle, which is about 10 % for $i = 0^\circ$ but increases up to 35% for $i = 60^\circ$.

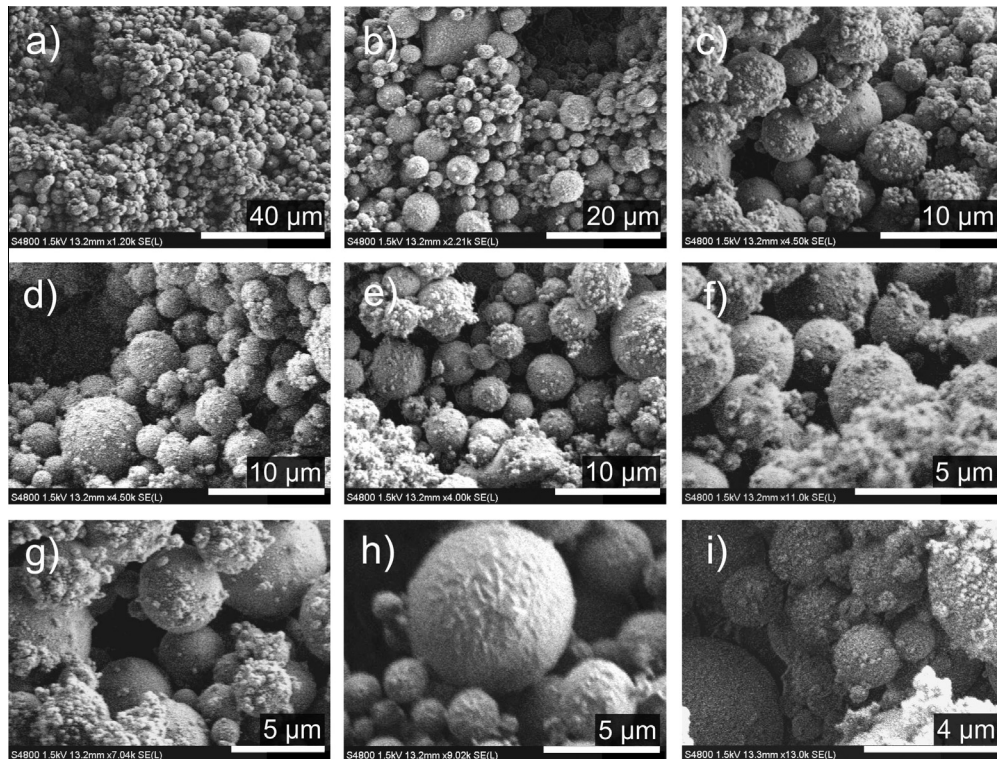


Fig. 4. Scanning electron microscope images of the micrometer-sized water ice particles. A detailed description of the used instrument is given by Voigt and Gorb (2010). The spatial scales of the images are shown by the thick wide scale bar in the lower right of the images and are: 40 μm (a), 20 μm (b), 10 μm (c), 10 μm (d), 10 μm (e), 5 μm (f), 5 μm (g), 5 μm (h) and 4 μm (i), respectively. Note that some of the spherical water ice particles are covered by frost (chips on the water ice particles), which had condensed on the sample's surface during the transfer, from the Dewar to the microscope.

Table 1

Overview of all measurements and configurations used in this work.

| | i (°) | Filters (nm) | Time resolution (min) | Total time (h) |
|---------------------|---------------|---------------------|-----------------------|----------------|
| Sample A 0–4 h | 0, 20, 40, 60 | 450, 750, 1064 | 50 | 4 |
| Sample B 0–2.5 h | 0, 40, 60 | 650, 1064 | 25 | 35 |
| 2.5–35 h | 0, 40, 60 | 450, 650, 750, 1064 | 110 | |
| Sample C 0–2 h | 0, 20, 40, 60 | 650 | 13 | 41 |
| 2–41 h | 0, 20, 40, 60 | 650 | 72 | |

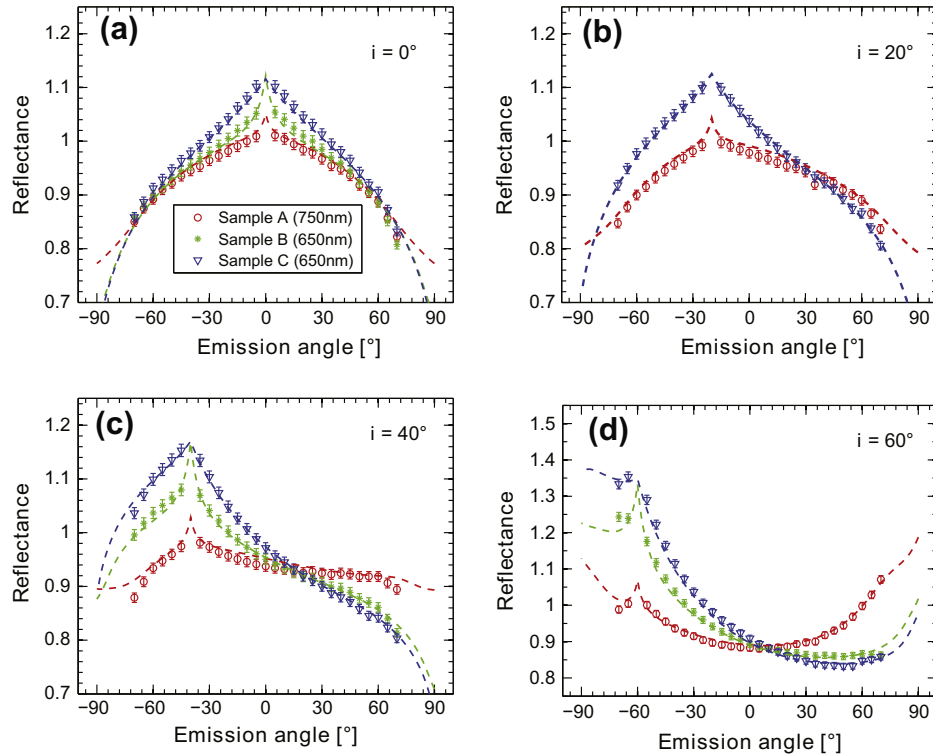


Fig. 5. The reflectance factor of fresh samples plotted as a function of emission angles. Four different incidence angles were used: $i = 0^\circ$ (a), $i = 20^\circ$ (b), $i = 40^\circ$ (c) and $i = 60^\circ$ (d). Measured data are plotted as symbols and results of fitting the experimental data by the Hapke model (3-parameter HG, version 1993) are overplotted as dotted lines. The significant differences between the photometric behaviors of the three fresh samples are discussed in Section 5.

While sample A shows lower values of reflectance than samples B and C at low phase angle, it shows significantly larger values of reflectance at high phase angle, with a relative difference of 25% at the maximum phase angle of 135° . Whereas samples B and C display remarkably similar behaviors at phase angles larger than 60° , they differ significantly at lower phase angle with a relative difference of reflectance of up to 10% and very contrasted evolutions of the phase curves at high incidence angle (opposite slopes between $e = -75^\circ$ and $e = -60^\circ$ for $i = 60^\circ$).

Fig. 6 shows a complete series of measurements performed with sample C at $i = 60^\circ$. The first and the last measurement are separated in time by 41 h. This figure illustrates the significant temporal evolution of the photometric properties of the samples. A continuous decrease with time of the reflectance at low phase angles is observed. Simultaneously, the reflectance at high phase angle continuously increases. A stable point is observed around $e = 5^\circ$, for which no temporal evolution is observed. The small irregularities between $e = +55^\circ$ and $e = 75^\circ$ are caused by a mechanical artifact of the instrument (see Section 2).

Figs. 7 and 8 complete Fig. 6 by showing five and six selected curves among the entire series of long-term measurements per-

formed with sample B (Fig. 7) and sample C (Fig. 8) at three incidence angles: $i = 0^\circ$, $i = 40^\circ$ and $i = 60^\circ$. The general behavior of sample C described in Fig. 5 is also observed for sample B. A continuous variation with time of the ratio between amounts of light scattered in the forward and backward directions is observed. However, there are some notable differences between the final stages of evolution of both samples. Sample B acquires with time a more strongly forward scattering behavior than sample C. This is especially obvious at $i = 60^\circ$ where sample B shows a higher reflectance at high phase angles by about 7%. Sample C always remains more reflective at low phase angle than at high phase angles, by about 10%.

Fig. 9 provides more quantitative estimates of these observations by showing the variations of the ratios between the reflectance in the forward scattering, $\text{Ref}(+70^\circ)$, and in the backward scattering directions, $\text{Ref}(-35^\circ)$ and $\text{Ref}(-55^\circ)$, with time. The upper panel shows the ratio between the reflectance at $e = -35^\circ$ and $e = +70^\circ$ for $i = 40^\circ$. The lower panel shows the ratio between $e = -55^\circ$ and $e = +70^\circ$ for $i = 60^\circ$. The decreases of these ratios with time represent shifts from backward to forward scattering. The initial values for these ratios vary by up to 50%. For $i = 40^\circ$ we see a

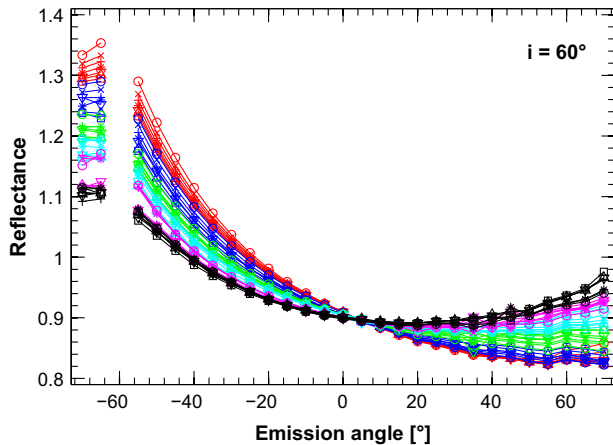


Fig. 6. Temporal evolution of the photometric behavior of sample C for $i = 60^\circ$. The first scan (also shown in this figure) appears in red. The highest reflectance is located in the back-scattering region (low phase angle) and the lowest reflectance is located in the forward-scattering region (high phase angle). The black curve was measured 41 h later. Between these two measurements, the temporal evolution is characterized by a continuous decrease of reflectance at low phase angle and a continuous increase of reflectance at high phase angle.

strong decline of the ratios during the first 4 h. The decrease is smaller and almost linear until the end for sample C. Sample B seems to reach a steady state after around 20 h. For $i = 60^\circ$, the situation is slightly different. The ratio of the forward to backward scattering of sample C declines nearly constantly while the ratio of sample B shows again a decline after 4 h. After this point, both samples show similar evolution.

The comparison of the measurements performed at the different wavelengths for samples A and B did not reveal significant spectral effects with the exception of the 1064 nm wavelength at which a slightly reduced reflectance and a slightly enhanced forward scattering behavior are observed. This behavior results from the slight absorption by water at this wavelength. Similar observations of the influence of measurement geometry on the absorption bands of water in hydrated minerals are discussed extensively by Pommerol and Schmitt (2008b).

5. Discussion

The multiple bidirectional reflectance measurements performed on the fresh micrometer-sized water ice samples all show the original photometric behavior of surfaces made of this material. In particular, all fresh samples behave completely differently from fresh snow, as measured in the field or in the laboratory (Middleton and Mungall, 1952; Aoki et al., 2000; Dumont et al., 2010; Pommerol et al., 2011). While snow always shows a very pronounced forward-scattering behavior and the absence of backscattering at phase angle larger than 5° , the micrometer-sized water ice shows the opposite behavior with a very strongly backscattering behavior and either an absent or very moderate forward-scattering depending on the sample.

We have systematically fitted our measured data by the Hapke photometric model as explained in Section 2 and as illustrated in Figs. 5, 7 and 8. The results of the fitting procedure are generally very satisfactory and the retrieved sets of Hapke parameters provided in Tables 2–7 can be used to reproduce the measured curves with high accuracy, interpolate the observed photometry to non-

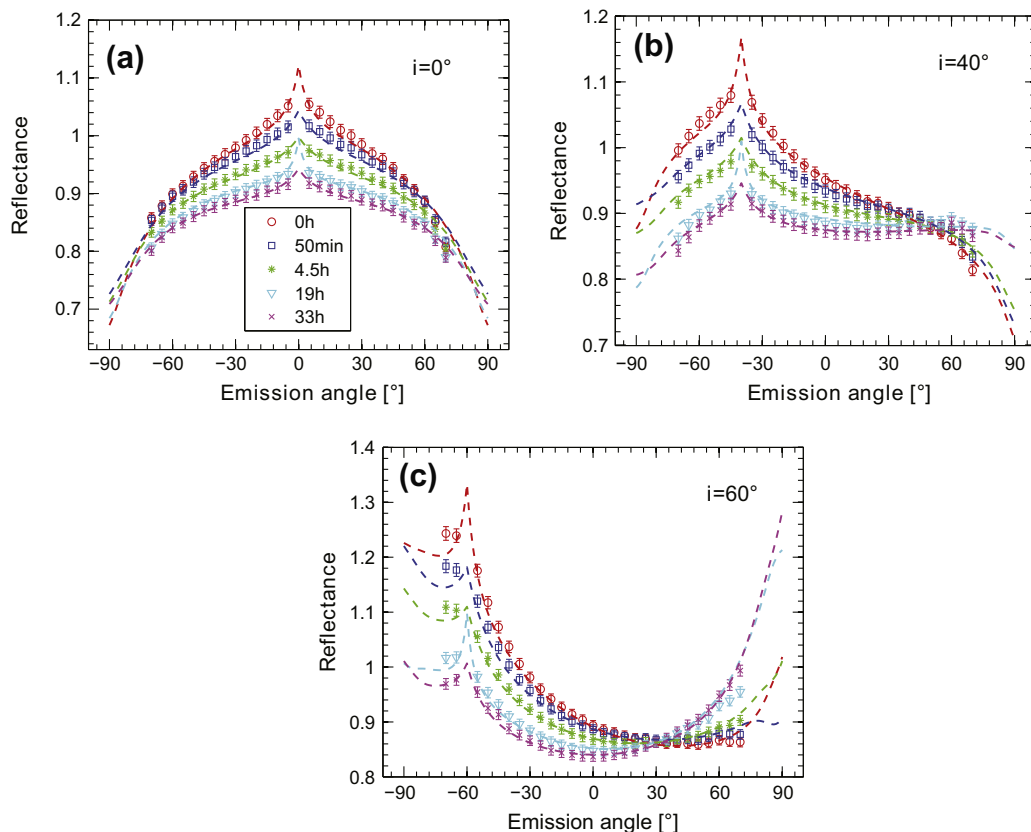


Fig. 7. Long-term temporal evolution of sample B. Five time-steps have been selected and are displayed for an incidence angle of 0° (a), 40° (b) and 60° (c). All plots are showing the same temporal evolution of the photometric behavior characterized by a decrease of reflectance at low phase angles and an increase at high phase angles.

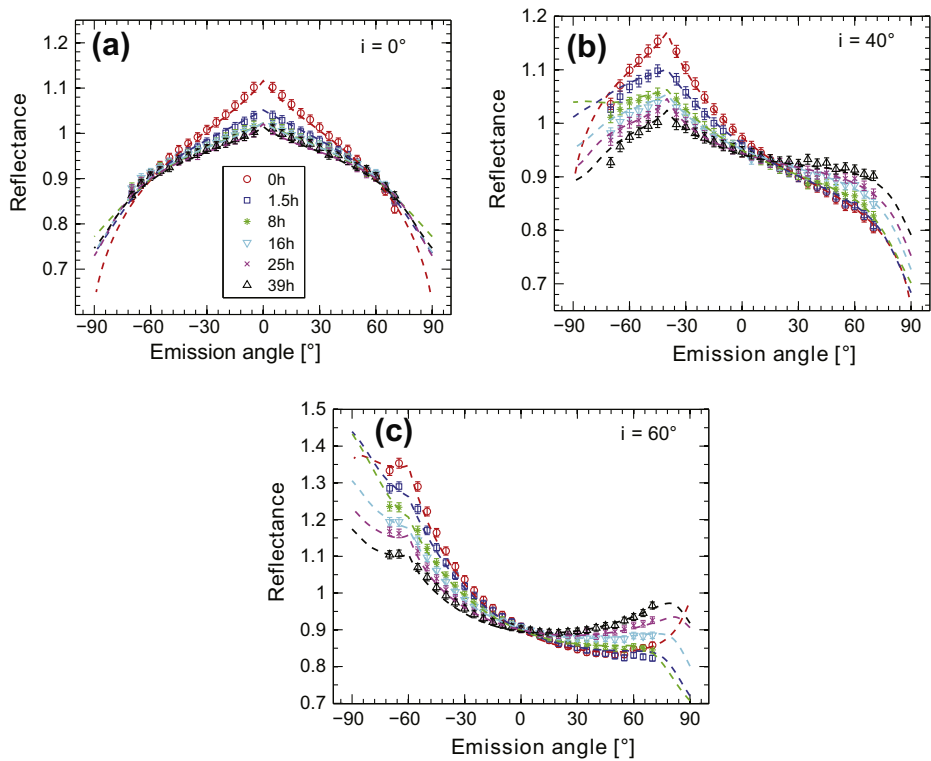


Fig. 8. Long-term temporal evolution of sample C. Five time-steps have been selected and are displayed for an incidence angle of 0° (a), 40° (b) and 60° (c). All plots show the same temporal evolution of the photometric behavior characterized by a decrease of reflectance at low phase angle and an increase at high phase angle. The fitted curves 3-parameter HG/v1993, parameters are provided in Table 6.

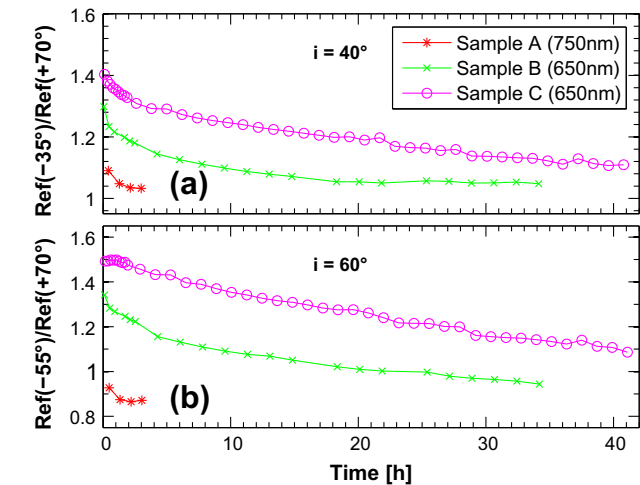


Fig. 9. Temporal evolution of the ratios of the reflectance at low phase angles (back-scattering) and at high phase angles (forward-scattering). The ratios are calculated for incidence angles of 40° (a) and 60° (b). The back-scattering point is always taken at a phase angle of 5° while the forward-scattering point is selected at a phase angle of 110° ($i = 40^\circ$, a) or 130° ($i = 60^\circ$, b).

measured geometries, and calculate other photometric properties such as hemispheric or geometric albedo.

While our fitting procedure permits good mathematical reproductions of the measured data, the physical meaning of the retrieved parameters is more questionable. Some of the parameters are poorly constrained and/or correlated. Similar observations with mineral samples and extensive discussions of the issues arising when trying to fit the Hapke model to measured data are proposed by Gunderson et al. (2006), Shepard and Helfenstein (2007, 2011) and Helfenstein and Shepard (2011).

Table 2
Fitted Hapke parameters (version 1993, 3-parameter HG) of the first scan of samples A (750 nm), B (650 nm) and C (650 nm). These parameter sets are plotted as dashed lines in Fig. 5. The 1 σ confidence intervals are $-0.0014/+0.0005$ (ω_0), -0.13 (h), $-0.34/+0.41$ (B_0), $+4$ (θ). Parameters $b/c/d$ are highly correlated and have no well defined confidence interval.

| | ω_0 | h | B_0 | θ | b | c | d | RMS | χ^2_v |
|----------|------------|------|-------|----------|------|-------|------|--------|------------|
| Sample A | 1.0000 | 0.03 | 0.47 | 8 | 0.34 | -0.41 | 0.26 | 0.0122 | 1.60 |
| Sample B | 0.9988 | 0.17 | 1.00 | 2 | 0.89 | 0.43 | 0.14 | 0.0164 | 2.70 |
| Sample C | 0.9983 | 0.25 | 0.89 | 0 | 0.87 | 0.44 | 0.21 | 0.0160 | 2.72 |

Table 3
Fitted Hapke parameters (version 2002) with 2-parameter HG-function (upper line) and 1-parameter HG-function (lower line) of the first scan of samples A (750 nm), B (650 nm) and C (650 nm). The 1 σ confidence intervals are $-0.0014/+0.0005$ (ω_0), -0.13 (h), $-0.34/+0.41$ (B_0), $+4$ (θ), $-0.14/0.07$ (b) and $+0.15$ (c) for 2-parameter HG, respectively ± 0.04 (b) for 1-parameter HG function.

| | ω_0 | h | B_0 | θ | b | c | RMS | χ^2_v |
|----------|------------|------|-------|----------|-------|-------|--------|------------|
| Sample A | 1.0000 | 0.01 | 0.64 | 2 | 0.30 | -0.48 | 0.0185 | 3.62 |
| | 1.0000 | 0.09 | 0.68 | 11 | 0.03 | | 0.0313 | 10.42 |
| Sample B | 0.9978 | 0.03 | 0.60 | 7 | 0.21 | 0.67 | 0.0292 | 9.17 |
| | 0.9976 | 0.05 | 0.62 | 8 | -0.16 | | 0.0271 | 7.85 |
| Sample C | 0.9977 | 0.07 | 0.51 | 10 | 0.24 | 0.91 | 0.0257 | 6.98 |
| | 0.9976 | 0.07 | 0.54 | 11 | -0.22 | | 0.0277 | 8.06 |

We note that the improved version of the Hapke model (Hapke, 2002) that incorporates anisotropic multiple scattering, what seems to be essential for high albedo samples, does not provide noticeably better fitting quality than the isotropic multiple scattering approximation (Hapke, 1993). The only differences are systematic shifts in some parameter values. However these shifts, except ω_0 , lie far inside the 1 σ confidence intervals. The choice of the sin-

Table 4

Hapke parameters of the selected measurements from sample B (650 nm), as plotted in Fig. 7. Fitted with 1993 version and 3-parameter HG. The 1σ confidence intervals are identical as in Table 2.

| | ω_0 | h | B_0 | θ | b | c | d | RMS | χ^2_v |
|--------|------------|------|-------|----------|------|------|------|--------|------------|
| 0 h | 0.9988 | 0.05 | 0.83 | 2 | 0.79 | 0.58 | 0.18 | 0.0235 | 6.00 |
| 50 min | 0.9989 | 0.13 | 0.80 | 5 | 0.89 | 0.61 | 0.10 | 0.0148 | 2.16 |
| 4.5 h | 0.9985 | 0.15 | 0.80 | 4 | 0.85 | 0.57 | 0.06 | 0.0113 | 1.28 |
| 19 h | 0.9985 | 0.03 | 0.76 | 2 | 0.37 | 0.08 | 0.12 | 0.0190 | 3.85 |
| 33 h | 0.9984 | 0.10 | 0.77 | 4 | 0.58 | 0.37 | 0.00 | 0.0111 | 1.24 |

Table 5

Hapke parameters of the selected data from sample B (650 nm), as plotted in Fig. 7. Fitted with 2002 version using 2-parameter HG function (upper line) and 1-parameter HG function (lower line). The 1σ confidence intervals are identical as in Table 3.

| | ω_0 | h | B_0 | θ | b | c | RMS | χ^2_v |
|--------|------------|------|-------|----------|-------|-------|--------|------------|
| 0 h | 0.9978 | 0.03 | 0.60 | 7 | 0.22 | 0.67 | 0.0292 | 9.17 |
| | 0.9976 | 0.05 | 0.62 | 8 | −0.16 | | 0.0272 | 7.85 |
| 50 min | 0.9980 | 0.03 | 0.57 | 7 | 0.17 | 0.65 | 0.0238 | 6.08 |
| | 0.9979 | 0.05 | 0.60 | 7 | −0.12 | | 0.0225 | 5.38 |
| 4.5 h | 0.9981 | 0.03 | 0.58 | 6 | 0.16 | 0.41 | 0.0216 | 5.03 |
| | 0.9980 | 0.05 | 0.61 | 8 | −0.08 | | 0.0199 | 4.22 |
| 19 h | 0.9987 | 0.03 | 0.57 | 6 | 0.17 | −0.19 | 0.0160 | 2.75 |
| | 0.9986 | 0.06 | 0.71 | 8 | 0.01 | | 0.0163 | 2.83 |
| 33 h | 0.9991 | 0.03 | 0.61 | 6 | 0.20 | −0.40 | 0.0151 | 2.45 |
| | 0.9991 | 0.06 | 0.80 | 10 | 0.05 | | 0.0179 | 3.41 |

Table 6

Hapke parameters of the selected measurements from sample C (650 nm), as plotted in Fig. 8. Fitted with 1993 version and 3-parameter HG function. For The 1σ confidence intervals see Table 2.

| | ω_0 | h | B_0 | θ | b | c | d | RMS | χ^2_v |
|-------|------------|------|-------|----------|------|-------|------|--------|------------|
| 0 h | 0.9983 | 0.25 | 0.89 | 0 | 0.87 | 0.44 | 0.21 | 0.0160 | 2.72 |
| 1.5 h | 0.9978 | 0.54 | 1.00 | 6 | 1.00 | 0.51 | 0.15 | 0.0123 | 1.61 |
| 8 h | 0.9983 | 0.59 | 1.00 | 9 | 1.00 | 0.57 | 0.11 | 0.0121 | 1.57 |
| 16 h | 0.9982 | 0.45 | 1.00 | 4 | 1.00 | 0.57 | 0.08 | 0.0101 | 1.08 |
| 27 h | 0.9984 | 0.18 | 0.59 | 3 | 0.87 | 0.87 | 0.08 | 0.0100 | 1.07 |
| 39 h | 0.9991 | 0.09 | 0.26 | 4 | 0.01 | −0.77 | 0.40 | 0.0083 | 0.74 |

Table 7

Hapke parameters of the selected measurements from sample C (650 nm), as plotted in Fig. 8. Fitted with 2002 version using 2-parameter HG function (upper line) and 1-parameter HG function (lower line). For the 1σ confidence intervals see Table 3.

| | ω_0 | h | B_0 | θ | b | c | RMS | χ^2_v |
|-------|------------|------|-------|----------|-------|------|--------|------------|
| 0 h | 0.9977 | 0.07 | 0.51 | 10 | 0.24 | 0.91 | 0.0257 | 6.98 |
| | 0.9976 | 0.07 | 0.54 | 11 | −0.22 | | 0.0277 | 8.06 |
| 1.5 h | 0.9964 | 0.15 | 0.52 | 9 | 0.11 | 1.92 | 0.0173 | 3.16 |
| | 0.9963 | 0.16 | 0.37 | 6 | −0.19 | | 0.0140 | 2.06 |
| 8 h | 0.9970 | 0.22 | 0.50 | 9 | 0.09 | 1.78 | 0.0136 | 1.95 |
| | 0.9975 | 0.31 | 0.48 | 10 | −0.14 | | 0.0135 | 1.91 |
| 16 h | 0.9980 | 0.19 | 0.51 | 8 | 0.09 | 1.24 | 0.0117 | 1.45 |
| | 0.9981 | 0.21 | 0.50 | 8 | −0.11 | | 0.0116 | 1.41 |
| 27 h | 0.9984 | 0.17 | 0.53 | 7 | 0.10 | 0.78 | 0.0104 | 1.15 |
| | 0.9983 | 0.16 | 0.55 | 7 | −0.08 | | 0.0108 | 1.22 |
| 39 h | 0.9992 | 0.12 | 0.47 | 6 | 0.14 | 0.13 | 0.0094 | 0.93 |
| | 0.9991 | 0.12 | 0.61 | 6 | −0.04 | | 0.0115 | 1.39 |

gle scattering phase function has a bigger influence. We compared RMS-values of different combinations of the two model versions and different Henyey–Greenstein formulations. This revealed that we reach highest fitting quality with a 3-parameter HG function

and the 1993 model version (RMS = 0.0107, average value of all 41 datasets from sample C). RMS-values are higher by about 20% when using a 1-parameter or 2-parameter HG function. RMS-values are slightly higher, by about 27%, when forcing the b and c parameters to lie on the hockey stick line defined by Hapke (2012). For purposes of data reproduction, the use of 3-parameter HG functions provides highest accuracy, but the 3 parameters are completely unconstrained. To compare the single particle phase functions to other data, the use of a 2-parameter HG-function is thus more appropriate.

We have independently fitted all steps from the time series measured for samples B and C, as well as for the short dataset of sample A, for which the low number of data points prevents a meaningful interpretation of the parameters evolutions (Fig. 10). In general, the dispersion of the values is smaller than what could be expected from the calculated 1σ confidence intervals (see Section 2.2). The single scattering albedo ω_0 (Fig. 10a) shows a slight increase with time for samples B and C. We have no element to determine, however, if this trend corresponds to a real physical evolution or is just a mathematical effect of parameters compensation in the fitting process. The mean slope angle θ shows similar behavior (Fig. 10d). The parameters that describe the opposition peak, B_0 and h , appear relatively stable despite the lack of data at this geometries and show no systematic trend (Fig. 10b and c). The most interesting parameters are the two Henyey–Greenstein parameters b and c (Fig. 10e and f), whose temporal evolution accounts for the observed trend from strong backward-scattering, just after production, towards more forward-scattering. We did not set an upper limit on the c parameter, because there is no theoretical limitation when b is close to 0 (see Fig. 2 in Hapke (2012)). Fig. 11 shows the two parameters b and c plotted against each other as a function of time. The starting points (fresh samples) lie on the right side of the hockey stick line. Sample B shifts almost horizontally to the left until a turning point and then moves down parallel to the hockey stick line. Sample C shows a strong initial increase of parameter c coupled to a decrease of parameter b , shifting the point to the upper left corner. The parameter c reaches maximum values of about 2.0 on the hockey stick line. After this point, the point moves downwards, parallel to the Hockey stick line but shifted to the left. As postulated by Hapke (2012), the hockey stick seems to have a certain width around the function defined in Eq. (4). This explains the slightly better fitting qualities when using a Henyey–Greenstein function with two independent parameters than when using Eq. (4) to relate b to c . We also notice that the fitting accuracy is significantly dependent on the evolution state of the samples. The most extreme example is sample C for which the RMS-values are rapidly decreasing during the first ten measurements. Afterwards, the decrease is slower but steady towards the last measurement. There is a factor of 3 between the highest and lowest RMS-values obtained for the first and last step of temporal evolution, respectively. The observed temporal evolution of the goodness of fit indicates a lower ability of the Hapke model to reproduce the strongly backscattering behavior of the fresh sample than the more forward-scattering behavior of the evolved sample. It is possible that difficulties to model the fresh micrometer-ice samples are due to the proximity of the average particle size to the wavelength of the light, a situation which is at the limit of the range of validity of the model.

It could seem reasonable at first view to attribute all initial differences between our samples (Fig. 5) to differences in surface roughness and/or filling factor. However, according to the model, the influence of roughness on reflectance is minor in the case of transparent samples and cannot account for the differences seen between our samples. We have experimentally verified this theoretical result by comparing the reflectance of two surfaces produced from 20- μ m glass spheres, one rough surface produced by

Table 8

Comparison of our sample (650 nm) to terrestrial snow types and icy satellites. Parameters sets of “snow frost” and “newly fallen snow” from Domingue et al. (1997), Enceladus (672 nm) and Europa (434 nm) from Verbisser et al. (2005).

| | ω_0 | h | B_0 | θ | b | c | d |
|--|------------|-------|-------|----------|-------|-------|------|
| Enceladus | 0.995 | 0.132 | 0.98 | 7 | −0.38 | | |
| Europa | 0.97 | 0.75 | 1.0 | 23 | −0.24 | | |
| Snow frost | 0.992 | 0.995 | 1.0 | 0 | 0.82 | 0.0 | |
| Newly fallen snow | 0.995 | 0.995 | 1.0 | 0 | 0.449 | 0.004 | |
| Micrometer-sized ice (first scan sample C) | 0.9983 | 0.25 | 0.89 | 0 | 0.87 | 0.44 | 0.21 |
| Micrometer-sized ice (sample C after 39 h) | 0.9991 | 0.09 | 0.26 | 4 | 0.01 | −0.77 | 0.40 |

sprinkling the fine powder, and one smooth surface obtained by slightly compacting the rough surface to make it perfectly smooth. As expected from the model, the observed difference was very minor. Variations in filling factor would only have an effect at low phase angle. In addition, we experimentally verified by applying different compactions to the samples that these effects are too subtle to explain the observed differences.

This leads to the conclusion that the three freshly produced sample materials were already different. Deviations as observed for sample A compared to samples B and C can only be explained by different scattering functions of the individual particles. Differences in the single particle scattering function could easily be explained by differences in the size and shape of the scatterers. It is very unlikely that the individual micrometer-sized particles differ between samples A, B and C because their production process was strictly identical. However, as described in Section 3.1., the individual particles tend to form agglomerates of different sizes. Although the scattering behavior is certainly dominated by the single particles, it is known that larger scale agglomerates also influence the photometric properties (Pommerol and Schmitt, 2008a). Because the formation of the agglomerates is, in turn, strongly influenced by subtle variations in the procedure used to prepare the surface from powder, our favorite hypothesis to explain the differences between the initial samples is the difference in the clustering of the individual particles to form larger-scale agglomerates.

Sintering of individual micrometer-sized particles is the only plausible explanation to the observed temporal evolution of the samples. We have also considered the possible contribution of frost condensation on the sample during their production and subsequent sublimation in the freezer. However, neither the timescale, intensity nor shape of the phase curves for potential influence of frost fit the observed evolution. By creating optical bonds between particles and by eventually changing conglomerates of small particles into individual large particles, sintering can explain the evolution of the single particle scattering as described in this paper.

Sintering of water ice particles is the morphological change of the material driven by the decrease of the surface energy of the system. Therefore, material is transported from the bulk particles to the neck regions, i.e. those regions where the particles are in contact. Due to the mass gain in the neck regions, the neck radius grows with time until an equilibrium neck radius is reached. The growth rate of the neck radius strongly depends on the temperature and on the physics of the transport process. For water ice, the most prominent transport effect is the mass transport caused by sublimation and recondensation of the material (vapor transport mechanism; Ratke et al., 1992). In general, the sintering mechanisms can be divided into two groups, surface transport and volume transport mechanisms (German, 1996). An overview of the different transport mechanisms can be found in Maeno and Eblnuma (1983) and Blackford (2007).

For small water ice particles (35 μm ; Fig. 10 in Blackford (2007)), only two surface transport mechanisms are important: evaporation–condensation (see Hobbs and Mason, 1964 or Maeno and Eblnuma, 1983) and surface diffusion. At low temperatures

(<215 K) and at early stages of the sintering process, when the neck radius is smaller than 10% of the particle radius, the surface diffusion process is dominant whereas at higher temperatures (>215 K) or during later stages of the sintering process, the evaporation–condensation process is more important. This process also strongly depends on the atmospheric pressure.

This implies that on icy satellites, such as Enceladus, where the temperatures is very low and the surface ice particles are freshly produced by the activity of the moon, the surface diffusion process determines the sintering of the ice particles. On Earth, both experiments (in Kiel and in Bern) were performed at relatively high temperatures (238 K). In this case, the evaporation–condensation process primarily influences the physical evolution of the samples. Due to the different pressure environments in the two laboratory experiments (vacuum conditions in Kiel and ambient pressure in Bern), the thermal evolutions of the samples are most probably not comparable.

We calculated the temporal evolution of the relative neck radius x/r of our micrometer-sized water ice particles at a temperature of 238 K using neck growth rates derived by Kossacki et al. (1994) and Ratke et al. (1992). For our particle radii, Kossacki et al. (1994) predicts a stationary relative neck radius of $x/r \sim 0.6$ reached after ~ 100 s. Ratke et al. (1992) arrive at a stationary relative neck radius of unity. However, the time needed to reach the relative neck radius of $x/r = 0.6$ is less than one hundred seconds.

Experimental studies of the sintering behavior of micrometer-sized water ice particles, conducted at the same temperature and pressure conditions as in our photometric measurements, are not directly available. Jellinek and Ibrahim (1967) investigated the decrease in surface area of powder made from spherical water ice particles with a radius of $r = 0.5 \mu\text{m}$ using the BET method at different temperatures (238–265 K). Pressure conditions are not specified. Their results indicate time scales of tens to hundreds of hours at temperature regimes similar to those of PHIRE-2. This range seems to be consistent with our measurements where no equilibrium state is reached within 40 h (Fig. 9).

Despite the fact that their physical meaning is unclear, the sets of Hapke parameters retrieved for the micrometer-sized ice particle samples and provided in Tables 2–7, can now be used for comparisons between the photometric properties of laboratory samples and the photometric properties of Solar System objects. Because of the large ranges of variability obtained for the various Hapke parameters when fitting the photometric model to the measured data, we do not attempt to directly compare the Hapke parameters obtained for different objects. Only the phase curves calculated from these parameters will now be discussed. We propose here a comparison with the reflectance curves of Enceladus and Europa, which are covered by high purity water ice with very fine particle size of some tens of microns. These surface material particles are about one order of magnitude larger than our artificially produced sample material. However, we see evidence that μm -sized ice particles form larger scale agglomerates during production. It is also possible that the particles that cover the surfaces of Enceladus and Europa are also agglomerates of finer particles.

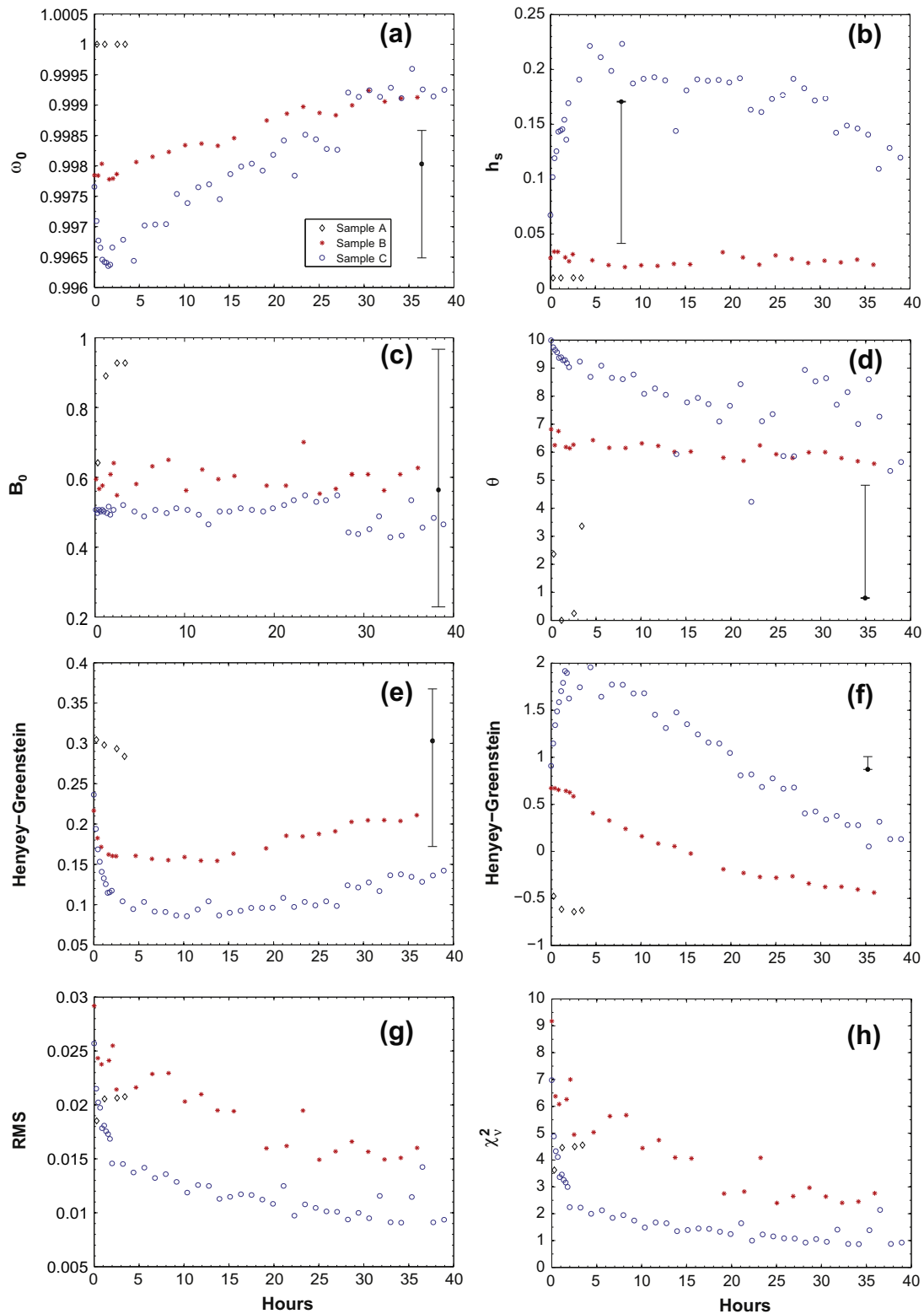


Fig. 10. Temporal evolution of Hapke model parameters ω_0 (a), h (b), B_0 (c), θ (d), b (e) and c (f) of samples A, B and C. The data are fitted with the 2002 version of the model and a 2-parameters Henyey–Greenstein function. The corresponding RMS and χ^2_v values are plotted in (g) and (h), respectively. For definitions of the model parameters see Section 2.2. The black dot with error bar represents the size of the confidence interval for each parameter as described in the last paragraph of Section 2.2.

In Fig. 12, we plot phase curves for sample C in its initial state (0 h) and after 39 h (same curves as in Fig. 8). We also show reflectance data for two types of terrestrial snow (“snow frost” and “newly fallen snow”) that have already been compared to the reflectance data of the jovian satellites by Domingue et al.

(1997). Finally we show phase curves for Enceladus (672 nm) and Europa (434 nm), calculated from Hapke coefficients determined by Verbiscer et al. (2005). To produce Fig. 12a, the Integrated Phase Function in units of magnitude was calculated by integrating the bidirectional reflection over the illuminated section

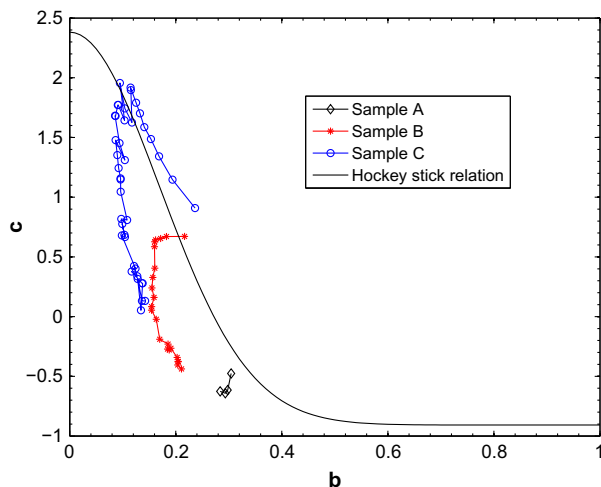


Fig. 11. Parameters b and c of the 2-term Henyey–Greenstein function (Eq. (2)) plotted for all temporal evolution states of micrometer sized ice samples. The parameter b describes the angular width of the scattering lobes, lower values meaning broader lobes. The parameter c is the ratio of the amplitudes of the backscattering and forward scattering lobes. The solid line indicates the Hockey stick relation defined by Hapke (2012) (see Eq. (4)).

of the planetary disk at a given phase angle, following Eq. (12.56) in Hapke (1993). Phase curves plotted for lab samples correspond to the phase curves of spherical planets homogeneously covered by a material with the same photometric properties as measured in the laboratory. The decrease of reflectance with phase angle is dominated by the decrease of the illuminated fraction of the disk. The effect of the anisotropy of light scattering at the surface appears as a secondary contribution to the phase curve that results in minor deviations from the ideal Lambertian case. In order to better visualize these deviations, we plot in Fig. 12b the ratios of the disk integrated phase functions of the different objects to the one of the ideal Lambertian case. The phase angle is restricted to $g > 2^\circ$ in both Fig. 12a and b, because of the absence of data at low phase angle in laboratory measurements.

As already mentioned, terrestrial snow appears relatively darker than the micrometer-sized ice particle samples and shows a very pronounced forward-scattering behavior and no backscattering peak. The surface of Enceladus shows an opposite behavior, strongly backscattering with no forward scattering peak. It also shows the highest absolute IPF values. The photometric behavior of the fresh micrometer-sized ice particle sample is much closer to the one of Enceladus than terrestrial snow. It shows a similar trend of continuously decreasing reflectance with phase angle, although the amplitude of the variations is much smaller, especially at low phase angle.

Europa appears darker than Enceladus because its surface is contaminated by minerals which lowers the albedo. The shapes of their phase curve are similar at high phase angle but Europa does not show such a strong increase of reflectance at phase angle lower than 50° as on Enceladus. The surface of Europa is as well darker than our unsintered micrometer-ice sample but shows a very similar shape of the phase curve. The sintered sample has a lot of similarities with terrestrial snow in terms of curve shape, but is brighter and a bit more backscattering. To our knowledge, the fresh samples of micrometer-sized water ice produced in these studies are the only reported ice samples whose photometric properties are able to reproduce to some extent the observed photometric behaviors of icy satellites.

The observation of rather different photometric behavior for samples composed purely of water ice has strong implication for remote-sensing observations of icy objects in the Solar System. It

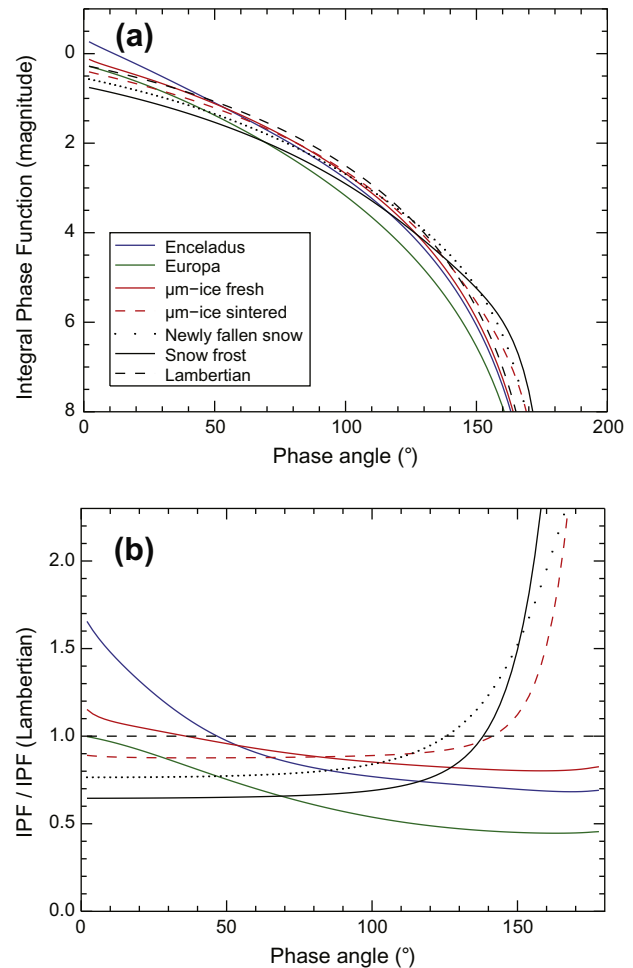


Fig. 12. Disk integrated phase function plotted versus phase angle (a) of Enceladus (675 nm), Europa (434 nm), unsintered micrometer sized ice (sample C, first scan, 650 nm), sintered micrometer sized ice (sample C, 39 h, 650 nm), newly fallen snow and snow frost. The Hapke parameters for the icy satellites are from Verbiscer et al. (2005), and the ones for snow from Domingue et al. (1997). All parameters are given in Table 8. Figure (b) shows the ratios between the curves plotted in (a) and the curve corresponding to the ideal Lambertian case.

is clear that, depending on the texture of the ice at the surface, the photometry of the studied object can be completely different, independent of the presence, amount and characteristics of other constituents. In the case of Europa and Enceladus, the comparison with samples composed of micrometer-sized water ice particles and snow provides additional indications to spectroscopic analyses (Hansen and Romain, 2012) that the size distribution of ice particles at the surface is dominated by such small particles. Large particles in the water ice fraction on Europa would result in significant forward scattering independent of mineral contamination and other surface constituents (see Carlson et al. (2009) for detailed description of Europa's surface composition). Additional experimental and theoretical work will be needed to permit the quantification of particle size from bidirectional reflectance data.

At the average temperature of the surface of Enceladus, 70 K, we calculated the typical timescale for ice sintering as 10^{18} years (according to formulas in Kossacki et al. (1994) and Ratke et al. (1992)), which means that no sintering will ever occur. This estimate is consistent with the observation that the phase curve of Enceladus looks similar, but even brighter and more backscattering than the one of freshly produced samples which experienced ambient conditions for some tens of seconds, until the first measurement was performed. The surface temperature on Enceladus can

however reach 145 K over the Tiger stripes at the South Pole (Spencer et al., 2006). In these conditions, sintering will occur with a typical timescale of 30 years, comparable to the deposition rate of ice particles at the surface as estimated by Kempf et al. (2010). The extent of this region is certainly too small to contribute significantly to the disk-integrated phase curve. However, disk resolved measurements assembled from images of the tiger stripes investigated by Annex et al. (2012) show a certain variety of surface textures, scattering properties and albedo between different locations inside the region. Analysis of near-infrared spectra by Porco et al. (2006), Jaumann et al. (2008) as well as Hansen and Romain (2012) show that particle sizes tend to be larger along the Tiger stripes compared to other surface regions.

The unique scattering behavior of micrometer-sized water ice and its temporal evolution have several implications for future observation campaigns. To detect potential forward-scattering peaks, phase angles larger than 120° are essential. Such extreme geometries as well as measurements near zero-phase can help in understanding the physical state of ice-bearing surfaces. As the backward-to-forward scattering ratio (see Fig. 9) of fine-grained ice can evolve with time as a result of sintering, measurements of this photometric criterion could permit a rough determination of the age of a surface, when the influence of other physical processes such as ice compaction by ion irradiation (e.g. Raut et al., 2007) or altering by high energy electron bombardment (Howett et al., 2011) is known.

In the case of comets, our experimental results are not directly applicable as the known exposed water ice deposits on 9P/Tempel 1 (Sunshine et al., 2006) contain only a few percent of pure ice, mixed with non-volatile components. The contaminant part has a major influence on photometric properties. However, the results of this study already tell us that it will be important to use realistic fine-grained ice when trying to produce analogs for cometary nuclei rather than terrestrial snow because their photometric properties strongly differ.

6. Conclusion

We have performed bidirectional reflectance measurements on three samples composed of pure micrometer-sized water ice produced in the exact same way. In their original state, these three samples show slightly different reflectance properties. Differences in surface roughness and compaction cannot account for this effect. We thus assume that different levels of clustering of individual particles to form larger agglomerates have a significant influence on the optical behavior. Despite these discrepancies, all samples produced from micrometer-sized water ice show remarkable scattering behavior with a dominant backscattering and the absence of a forward scattering peak. This photometric behavior is radically different from that of different types of terrestrial snow.

The samples show a significant evolution of their scattering properties with time with a steady evolution rate, independent of the initial properties. Backscattering decreases with time, while forward scattering increases. This temporal evolution is thought to originate from sintering processes, where optical bonds between single particles are created.

We have fitted all measurements with the Hapke model and provide parameters to reproduce our data for comparison with other samples and astronomical observations. First-order comparisons with Enceladus and Europa, which are known to contain ice particles in the micrometer range (Hansen and Romain, 2012), show a much better agreement between the photometric behavior of these satellites and the micrometer-sized ice particle sample than with terrestrial snow (Domingue et al., 1997). The strong evolution of the forward-to-backward scattering ratio as a result of ice

sintering offers opportunities for rapid assessment of the physical state and age of icy surfaces from visible bidirectional reflectance measurements when the environmental conditions are known. Future experimental and theoretical work will be necessary to permit more quantitative interpretations of photometric observations. Furthermore it is not clear at the moment if the drastically different microphysical processes involved in the sintering under terrestrial conditions and at the surface of outer Solar System objects results in the same photometric changes of the investigated sample material. Future measurements of similar samples evolved in low-temperature and low-pressure environments inside simulation chambers will be necessary to elucidate this question.

Acknowledgments

The quality of this manuscript benefited from very useful comments and suggestions by two anonymous reviewers. The construction of the Planetary Ice Laboratory was funded equally by the University of Bern and The Swiss National Science Foundation (SNSF Project #206021_133827).

Bastian Gundlach is partially supported by the DFG SPP 1573 under Grant BI298/19-1.

References

- A'Hearn, M.F. et al., 2005. Deep Impact: Excavating Comet Tempel 1. *Science* 310, 258–264.
- A'Hearn, M.F. et al., 2011. EPOXI at Comet Hartley 2. *Science* 332, 1396–1400.
- Annex, A., Verbiscer, A., Helfenstein, P., 2012. Photometric Properties of Enceladus' South Polar Terrain. *American Astronomical Society. DPS Meeting #44*, #112.10.
- Aoki, T., Aoki, T., Fukabori, M., Hachikubo, A., Tachibana, Y., Nishio, F., 2000. Effects of snow physical parameters on spectral albedo and bidirectional reflectance of snow surface. *J. Geophys. Res.* 105, 10219–10236.
- Beck, P., Pommerol, A., Thomas, N., Schmitt, B., Moynier, F., Barrat, J.-A., 2012. Photometry of meteorites. *Icarus* 218, 364–377.
- Blackford, J.R., 2007. Sintering and microstructure of ice: A review. *J. Phys. D: Appl. Phys.* 40, R355–R385.
- Buratti, B.J., 1995. Photometry and surface structure of the icy Galilean satellites. *J. Geophys. Res.* 100, 19061–19066.
- Carlson, R. et al., 2009. Europa's surface composition. In: Pappalardo, R. et al. (Eds.), *Europa*. University of Arizona Press, pp. 283–327. ISBN: 9780816528448.
- Cruikshank, D., Morrison, D., Pilcher, C., 1977. Identification of a new class of satellites in the outer Solar System. *Astrophys. J.* 217, 1006–1010.
- Domingue, D., Verbiscer, A., 1997. Re-analysis of the solar phase curves of the icy Galilean satellites. *Icarus* 128, 49–74.
- Domingue, D., Hapke, B., Lockwood, G., Thompson, D., 1991. Europa's phase curve – Implications for surface structure. *Icarus* 90, 30–42.
- Domingue, D., Hartman, B., Verbiscer, A., 1997. The scattering properties of natural terrestrial snows versus icy satellite surfaces. *Icarus* 128, 28–48.
- Dumont, M., Brissaud, O., Picard, G., Schmitt, B., Gallet, J.-C., Arnaud, Y., 2010. High accuracy measurements of snow bidirectional reflectance distribution function at visible and NIR wavelengths – Comparison with modeling results. *Atmos. Chem. Phys.* 10, 2507–2520.
- Emery, J., Burr, D., Cruikshank, D., Brown, R., Dalton, J., 2005. Near infrared 0.8–4.0 μm spectroscopy of Mimas, Enceladus, Thetys, and Rhea. *Astron. Astrophys.* 435, 353–362.
- Filacchione, G., Capaccioni, F., McCord, T., Coradini, A., Cerroni, P., Bellucci, G., Tosi, F., D'Aversa, E., Formisano, V., Brown, R., Baines, K., Bibring, J., Buratti, B., Clark, R., Combes, M., Cruikshank, D., Drossart, P., Jaumann, R., Langevin, Y., Matson, D., Mennella, V., Nelson, R., Nicholson, P., Sicardy, B., Sotin, C., Hansen, G., Hibbitts, K., Showalter, M., Newman, S., 2007. Saturn's icy satellites investigated by Cassini-VIMS. I. Full-disk properties: 350–5100 nm reflectance spectra and phase curves. *Icarus* 186, 259–290.
- Filacchione, G., Capaccioni, F., Clark, R., Cuzzi, J., Cruikshank, D., Coradini, A., Cerroni, P., Nicholson, P., McCord, T., Brown, R., Buratti, B., Tosi, F., Nelson, R., Jaumann, R., Stephan, K., 2010. Saturn's icy satellites investigated by Cassini-VIMS. II. Results at the end of nominal mission. *Icarus* 206, 507–523.
- German, R., 1996. *Sintering Theory and Practice*. John Wiley and Sons, Inc., New York.
- Gunderson, K., Thomas, N., Whitby, J.A., 2006. First measurements with the Physikalisches Institut Radiometric Experiment (PHIRE). *Planet. Space Sci.* 54, 1046–1056.
- Gunderson, K., Lüthi, B., Russel, P., Thomas, N., 2007. Visible/NIR photometric signatures of liquid water in martian regolith simulant. *Planet. Space Sci.* 55, 1272–1282.
- Gundlach, B., Kilias, S., Beitz, E., Blum, J., 2011. Micrometer-sized ice particles for planetary-science experiments – I. Preparation, critical rolling friction force, and specific surface energy. *Icarus* 214, 717–723.

- Hansen, G., McCord, T., 2004. Amorphous and crystalline ice on the Galilean satellites: A balance between thermal and radiolytic processes. *J. Geophys. Res.* 109, E01012.
- Hansen, G.B., Romain, J., 2012. Modeling of layers of micron sized water ice over Enceladus surface to fit the 1–5 μm spectra from the Cassini VIMS instrument. *Lunar Planet. Sci.* 43, Abstract #2625.
- Hapke, B., 1981. Bidirectional reflectance spectroscopy. 1. Theory. *J. Geophys. Res.* 86, 3039–3054.
- Hapke, B., 1986. Bidirectional reflectance spectroscopy. 4. Extinction and the Opposition Effect. *Icarus* 88, 407–417.
- Hapke, B., 1993. Theory of Reflectance and Emittance Spectroscopy: Topics in Remote Sensing. Cambridge, UK, pp. 317–318.
- Hapke, B., 2002. Bidirectional reflectance spectroscopy. 5. The coherent backscatter Opposition Effect and anisotropic scattering. *Icarus* 157, 523–534.
- Hapke, B., 2012. Bidirectional reflectance spectroscopy. 7. The single particle phase function Hockey stick relation. *Icarus* 221, 1079–1083.
- Hapke, B., Shepard, M.K., Nelson, R., Smythe, W., Piatek, J., 2009. A quantitative test of the ability of models based on the equation of radiative transfer to predict the bidirectional reflectance of a well-characterized medium. *Icarus* 199, 210–218.
- Helfenstein, P., Shepard, M.K., 2011. Testing the Hapke photometric model: Improved inversion and the porosity correction. *Icarus* 215, 83–100.
- Hendrix, A.R., Buratti, B.J., 2009. Multi-wavelength photometry of the icy Saturnian satellites: A first look. *Lunar Planet. Sci.* 40, Abstract 2722.
- Heney, L.G., Greenstein, J.L., 1941. Diffuse radiation in the Galaxy. *Astrophys. J.* 93, 70–83.
- Hobbs, P., Mason, B., 1964. The sintering and adhesion of ice. *Philos. Mag.* 9, 181–197.
- Howett, C., Spencer, J., Schenk, P., Johnson, R., Paranic, C., Hurford, T., Verbiscer, A., Segura, M., 2011. A high-amplitude thermal inertia anomaly of probable magnetospheric origin on Saturn's moon Mimas. *Icarus* 216, 221–226.
- Jaumann, R., Stephan, K., Hansen, G., Clark, R., Buratti, B., Brown, B., Baines, K., Newman, S., Bellucci, G., Filacchione, G., Coradini, A., Cruikshank, D., Griffith, C., Hibbitts, C., McCord, T., Nelson, R., Nicholson, P., Sotin, C., Wagner, R., 2008. Distribution of icy particles across Enceladus' surface as derived from Cassini-VIMS measurements. *Icarus* 193, 407–419.
- Jellinek, H.H.G., Ibrahim, S.H., 1967. Sintering of powdered ice. *J. Colloid Interface Sci.* 25, 245–254.
- Johnson, J.R. et al., 2006. Spectroscopic properties of material observed by Pancam on the Mars Exploration Rovers: 1. Spirit. *J. Geophys. Res.* 111, E02S14.
- Kempf, S., Beckmann, U., Schmidt, J., 2010. How the Enceladus dust plume feeds Saturn's E ring. *Icarus* 206, 446–457.
- Kennedy, J., Eberhart, R.C., 1995. Particle Swarm Optimization. In: Proceedings of IEEE International Conference on Neural Networks, Piscataway, NJ, pp. 1942–1948.
- Kossacki, K.J., Kömle, N.I., Kargl, G., Steiner, G., 1994. The influence of grain sintering on the thermoconductivity of porous ice. *Planet. Space Sci.* 42, 383–389.
- Li, J.Y., A'Hearn, M., Farnham, T., McFadden, L., 2009. Photometric analysis of the nucleus of Comet 81P/Wild 2 from Stardust images. *Icarus* 204, 209–226.
- Maeno, N., Eblnuma, T., 1983. Pressure sintering of ice and its implication to the densification of snow at polar glaciers and ice sheets. *J. Phys. Chem.* 87, 4103–4110.
- Markwardt, C.B., 2008. In: Bohlender, D.A., Durand, D., Dowler, P. (Eds.), Non-Linear Least Squares Fitting in IDL with MPFIT, vol. 441. Astronomical Society of the Pacific Conference Series, pp. 251–254.
- McGuire, A., Hapke, B., 1995. An experimental study of light scattering by large, irregular particles. *Icarus* 113, 134–155.
- Middleton, W., Mungall, A., 1952. The luminous directional reflectance of snow. *J. Opt. Soc. Am.* 42, 572–579.
- Newman, S.F., Buratti, B.J., Brown, R.H., Jaumann, R., Bauer, J., Momary, T., 2008. Photometric and spectral analysis of the distribution of crystalline and amorphous ices on Enceladus as seen by Cassini. *Icarus* 193, 397–406.
- Nicholson, P.D. et al., 1996. Observations of Saturn's ring plane crossing in August and November 1995. *Science* 272, 509–516.
- Pommerol, A., Schmitt, B., 2008a. Strength of the water near-infrared absorption bands in hydrated minerals: Effects of particle size and correlation with albedo. *J. Geophys. Res.* 113, E10009. <http://dx.doi.org/10.1029/2007JE003069>.
- Pommerol, A., Schmitt, B., 2008b. Strength of the water near-infrared absorption bands in hydrated minerals: Effects of measurement geometry. *J. Geophys. Res.* 113, E12008. <http://dx.doi.org/10.1029/2008JE003197>.
- Pommerol, A., Thomas, N., Affolter, M., Portyankina, G., Jost, B., Aye, K.-M., 2011. Photometry and bulk physical properties of Solar System surfaces icy analogs: The Planetary Ice Laboratory at University of Bern. *Planet. Space Sci.* 59, 1601–1612.
- Porco, C. et al., 2006. Cassini observes the active South Pole of Enceladus. *Science* 311, 1393–1401.
- Ratke, L., Kochan, H., Thomas, H., 1992. Laboratory studies on cometary crust formation: The importance of sintering. *Asteroids Comets Meteors*, 497–500.
- Raut, U., Teolis, B., Loeffler, M., Vidal, R., Farmá, M., Baragiola, R., 2007. Compaction of microporous amorphous solid water by ion irradiation. *J. Chem. Phys.* 126, 244511–244515.
- Rodríguez, S. et al., 2007. Enceladus regional photometric properties from ISS/Cassini images. *Bull. Am. Astron. Soc.* 38, 495.
- Schmidt, J., Brilliantov, N., Spahn, F., Kempf, S., 2008. Slow dust in Enceladus' plume from condensation and wall collisions in tiger stripe fractures. *Nature* 451, 685–688.
- Shepard, M.K., Helfenstein, P., 2007. A test of the Hapke photometric model. *J. Geophys. Res.* 112, E03001. <http://dx.doi.org/10.1029/2005JE002625>.
- Shepard, M.K., Helfenstein, P., 2011. A laboratory study of the bidirectional reflectance from particulate samples. *Icarus* 215, 526–533.
- Showalter, M., Cuzzi, J., Larson, S., 1991. Structure and particle properties of Saturn's E ring. *Icarus* 94, 451–473.
- Souchon, A.L. et al., 2011. An experimental study of Hapke's modeling of natural granular surface samples. *Icarus* 215, 313–331.
- Spencer, J.R. et al., 2006. Cassini encounters Enceladus: Background and the discovery of a South Polar hot spot. *Science* 311, 1401–1405.
- Sunshine, J.M. et al., 2006. Exposed water ice deposits on the surface of Comet 9P/Tempel 1. *Science* 311, 1453–1455.
- Sunshine, J.M., Groussin, O., Schultz, P., A'Hearn, M., Feaga, L., Farnham, T., Klaasen, K., 2007. The distribution of water ice in the interior of Comet Tempel 1. *Icarus* 190, 284–294.
- Verbiscer, A., Veverka, J., 1990. Scattering properties of natural snow frost – Comparison with icy satellite photometry. *Icarus* 88, 418–428.
- Verbiscer, A., Helfenstein, P., Veverka, J., 1990. Backscattering from frost on icy satellites in the outer Solar System. *Nature* 347, 162–164.
- Verbiscer, A.J., French, R.J., McGhee, C.A., 2005. The opposition surge of Enceladus: HST observations 338–1022 nm. *Icarus* 173, 66–83.
- Verbiscer, A., Peterson, D., Skrutskie, M., Cushing, M., Helfenstein, P., Nelson, M., Smith, J., Wilson, J., 2006. Near-infrared spectra of the leading and trailing hemispheres of Enceladus. *Icarus* 182, 211–223.
- Voigt, D., Gorb, S., 2010. Egg attachment of the asparagus beetle *Crioceris asparagi* to the crystalline waxy surface of *asparagus officinalis*. *Proc. Biol. Sci.* 277, 895–903.
- Wada, K., Tanaka, H., Suyama, T., Kimura, H., Yamamoto, T., 2008. Numerical simulation of dust aggregate collisions. II. Compression and disruption of three-dimensional aggregates in head-on collisions. *Astrophys. J.* 677, 1296–1308.
- Zhang, H., Voss, K., 2011. On Hapke photometric model predictions on reflectance of closely packed particulate surfaces. *Icarus* 215, 27–33.